

Characteristics of gravity wave horizontal phase velocity spectra in the mesosphere over the Antarctic stations, Syowa and Davis.

Masaru Kogure¹, Nakamura Takuji², Damian Murphy³, Michael J. Taylor⁴, Yucheng Zhao⁴, Pierre-Dominique Pautet⁵, Masaki Tsutsumi², Yoshihiro Tomikawa², Mitsumu K. Ejiri², and Takanori Nishiyama²

¹Kyushu University

²National Institute of Polar Research

³Australian Antarctic Division

⁴Utah State University

⁵Utah State University

November 23, 2022

Abstract

Mesospheric gravity-wave (GW) phase velocity spectra and total powers at two Antarctic stations, Davis and Syowa, were derived using OH airglow image data from March to October in 2016. The total powers have similar seasonal variation, that is, maxima in winter at both stations. However, the power at Davis was one standard deviation larger in winter and three times smaller in September than at Syowa. The total power at Davis in winter was mainly attributed to GWs with high eastward (phase velocity). On the other hand, the higher total power at Syowa in September was attributed to GWs with omnidirectional phase velocity. These differences between Syowa and Davis can not be explained by the wind filtering effect, and other factors are needed. To further explore the origin of the difference in winter, we focused on an event on August 29, 2016, in which GWs with $\sim 100 \text{ ms}^{-1}$ southeastward phase velocity appeared at Davis. The raytracing method was applied, and its result indicated that those GWs with high southeastward phase velocity propagated from $\sim 45 \text{ km}$ altitude over the southern ocean (where GWs with high amplitude and southeastward propagating emitted from the tropospheric jet appeared. These jet GWs were probably saturated in 45-50 km altitudes. Therefore, the GWs with eastward phase velocity were probably secondary gravity waves. This result suggests that the higher power in the eastward high phase velocity domain at Davis was contributed to by secondary GWs.

1
2 **Characteristics of gravity wave horizontal phase velocity spectra in the mesosphere**
3 **over the Antarctic stations, Syowa and Davis**

4 **Masaru Kogure¹, Takuji Nakamura^{2,3}, Damian J. Murphy⁴, Michael J. Taylor⁵, Yucheng**
5 **Zhao⁵, Pierre-Dominique Pautet⁵, Masaki Tsutsumi^{2,3}, Yoshihiro Tomikawa^{2,3}, Mitsumu K.**
6 **Ejiri^{2,3}, Takanori Nishiyama^{2,3}**

7 ¹ Department of Earth and Planetary Science, Kyushu University, Fukuoka, Japan.

8 ² National Institute of Polar Research.

9 ³ Department of Polar Science, SOKENDAI (The Graduate University for Advanced Studies),
10 Tachikawa, Japan.

11 ⁴ Australian Antarctic Division, Department of Agriculture, Water and the Environment,
12 Kingston, Australia.

13 ⁵ Center for Atmospheric and Space Sciences/Physics Department, Utah State University, Logan,
14 UT, USA.

15
16 Corresponding author: Masaru Kogure (kogure.masaru.695@m.kyushu-u.ac.jp)

17 **Key Points:**

- 18 • Mesospheric gravity-wave activity at two Antarctic stations was larger in winter than in
19 spring and fall.
- 20 • The wave activity at Davis was larger in winter than Syowa but smaller in fall, which
21 cannot be explained by the wind filtering effect.
- 22 • We demonstrated that gravity waves with $\sim 100 \text{ ms}^{-1}$ eastward phase velocity at Davis
23 were generated by primary gravity wave breaking.
24

25 **Abstract**

26 Mesospheric gravity-wave (GW) phase velocity spectra and total powers at two Antarctic
27 stations, Davis and Syowa, were derived using OH airglow image data from March to October in
28 2016. The total powers have similar seasonal variation, that is, maxima in winter at both stations.
29 However, the power at Davis was one standard deviation larger in winter and three times
30 smaller in September than at Syowa. The total power at Davis in winter was mainly attributed to
31 GWs with high eastward ($\geq \sim 50 \text{ ms}^{-1}$) phase velocity. On the other hand, the higher total
32 power at Syowa in September was attributed to GWs with omnidirectional phase velocity. These
33 differences between Syowa and Davis can not be explained by the wind filtering effect, and other
34 factors are needed. To further explore the origin of the difference in winter, we focused on an
35 event on August 29, 2016, in which GWs with $\sim 100 \text{ ms}^{-1}$ southeastward phase velocity appeared
36 at Davis. The raytracing method was applied, and its result indicated that those GWs with high
37 southeastward phase velocity propagated from $\sim 45 \text{ km}$ altitude over the southern ocean
38 ($\sim 43^\circ\text{E}$, $\sim 58^\circ\text{S}$) where GWs with high amplitude and southeastward propagating emitted from
39 the tropospheric jet appeared. These jet GWs were probably saturated in 45-50 km altitudes.
40 Therefore, the GWs with eastward phase velocity were probably secondary gravity waves. This
41 result suggests that the higher power in the eastward high phase velocity domain at Davis was
42 contributed to by secondary GWs.

43

44 **1 Introduction**

45 Gravity waves (GW) play an essential role in transporting momentum vertically and
46 driving the circulation in the middle atmosphere (Fritts and Alexander, 2003). Current global

47 circulation models (GCMs) cannot resolve the full spectrum of GWs so that GW influences (GW
48 drags) are parametrized in GCMs. Although the GW drag parameterization schemes improve the
49 ability of GCMs to reproduce observations, they still poorly represent GW sources, spectra, local
50 variability, and intermittency, which causes deviations between GCMs and the real atmosphere
51 (Alexander et al., 2010). Inadequate knowledge of GWs is a key element of this limitation.

52 In order to understand GW sources and features, many studies have investigated GWs in
53 the real atmosphere by using in-situ and remote sensing instruments. Airglow imaging is one
54 remote sensing method that has high sensitivity to GWs with small horizontal wavelengths (~10s
55 km) and short periods (several minutes). Such GWs deposit substantial momentum around the
56 mesopause (Fritts and Vincent, 1987).

57 Matsuda et al. (2017) investigated the spatial variability of GW horizontal phase velocity
58 around the edge of Antarctica by using observations from four OH airglow imagers during 1.5
59 months (April to May) at Syowa (69°S, 40°E), Davis (69°S, 78°E), McMurdo (78°S, 167°E), and
60 Halley (76°S, 26°E). These instruments which are operated by the Antarctic Gravity Wave
61 Instrument Network (ANGWIN) showed that GW intermittency can be caused by the wind
62 filtering effect, and the GW activity over the Antarctic was variable in latitude (the GW activities
63 at Syowa and Davis were ~5 times larger than those at McMurdo and Halley). They also found
64 that GW power spectral density (PSD) in eastward phase velocity less than $\sim 70 \text{ ms}^{-1}$ was ~10
65 times larger at Davis than at Syowa. This large PSD at Davis was exceptional because the GWs
66 with small eastward phase velocity could not reach the airglow layer from the troposphere at
67 Davis, as well as Syowa. The paper mentioned that a possible source of those GWs may be
68 secondary generation above the stratosphere, although it does not robustly demonstrate the

69 possible source. Also, it is uncertain that the large PSD in the eastward velocity is a common
 70 feature at Davis because of the short (1.5 month) dataset.

71 The purpose of this study is to clarify differences in phase velocity spectra between Davis
 72 and Syowa and to show statistically significant results by using a whole Austral winter season
 73 (March to October) in 2016. Chapter 2 introduces OH airglow imagers at Syowa and Davis, and
 74 data analysis. In Chapter 3, we show the differences of GW activities between Syowa and Davis,
 75 and compare our results with Matsuda et al. (2017). We discuss the effects of wind filtering on
 76 the GWs in Chapter 4 and investigate a source of GWs with eastward phase velocity at Davis.

77 **2. Observation and Data analysis.**

78 Two OH airglow imagers at Syowa (40°E, 69°S) and Davis (78°E, 69°S) are operated by
 79 National Institute of Polar Research (NIPR) and the Utah State University, respectively. Both
 80 imagers are equipped with indium gallium arsenide (InGaAs) detectors, which are sensitive to
 81 wavelengths between 0.9-1.7 μm , avoiding a large part of the auroral contamination (0.4-0.8 μm)
 82 seen by CCD detectors (Matsuda et al., 2017). The detectors are incorporated with a Fujinon
 83 FE185C086HA-1 C-mount fisheye lens to observe the whole sky. The specification of both

Station	Latitude	Longitude	Operation Institution	Airglow ^a	Sampling Interval ^b	Exposure	Detector Size
Syowa	69° S	40° E	NIPR	OH (0.9-1.7 μm)	5 s	2 s	320×256
Davis	69° S	78° E	USU	OH (0.9-1.7 μm)	10 s	3 s	320×256

^a The OH layer altitude is assumed as 87 km.

^b OH intensity images are averaged in 1 min.

84 imagers is summarized in Table 1.

85

86 Table 1. Summary of the two airglow imager specifications.

87

88 This study used the data without clouds, moon, and auroral contamination lasting for more than 1
 89 hour from March to October 2016. Table 2 shows the distribution of the data windows, and this
 90 study analyzed 39 days at Syowa and 55 days at Davis.

		Mar.	Apr.	May	Jun.	Jul.	Aug.	Sep.	Oct.	Total
Syowa	Num. of night	1	8	9	3	4	7	6	1	39
	Total length (hour)	1.0	17.9	35.7	11.4	14.8	23.5	12.2	1.3	117.5
Davis	Num. of night	6	6	7	2	8	11	10	5	55
	Total length (hour)	15.4	12.3	15.8	12.8	26.0	56.0	27.6	10.6	176.5

91

92 Table 2. The number of data windows used in this study. The criteria for choosing the data are
 93 (1) clear-sky, (2) without the moon, and (3) aurora-free images continued for > 1 hour.

94

95 To derive a GW phase velocity spectrum, an M-transform was applied to the OH airglow
 96 image data. Since the M-transform is described in Matsuda et al. (2014; 2017) and Perwitasari et
 97 al. (2018) in detail, only preprocesses are explained here. The raw image data were averaged to 1
 98 min for compatibility between measurement cadences at Syowa and Davis and star and dark
 99 count removal was applied. To derive relative OH airglow intensity perturbations, the average
 100 night time intensity is subtracted from each 1 min image, the residual intensity (I') was divided
 101 by the nightly mean (I_0), and then I'/I_0 was defined as the relative intensity perturbation. The
 102 I'/I_0 images were projected onto geographical coordinates, assuming a mean emission height of
 103 87 km altitude (Baker and Stair, 1988). An OH emission height can vary between 79-88 km
 104 altitudes (Grygalashvyly et al., 2014; Nishiyama et al., 2021), but this causes less than 10 %
 105 phase speed error and the error can be neglected in this study. The M-transform was applied to

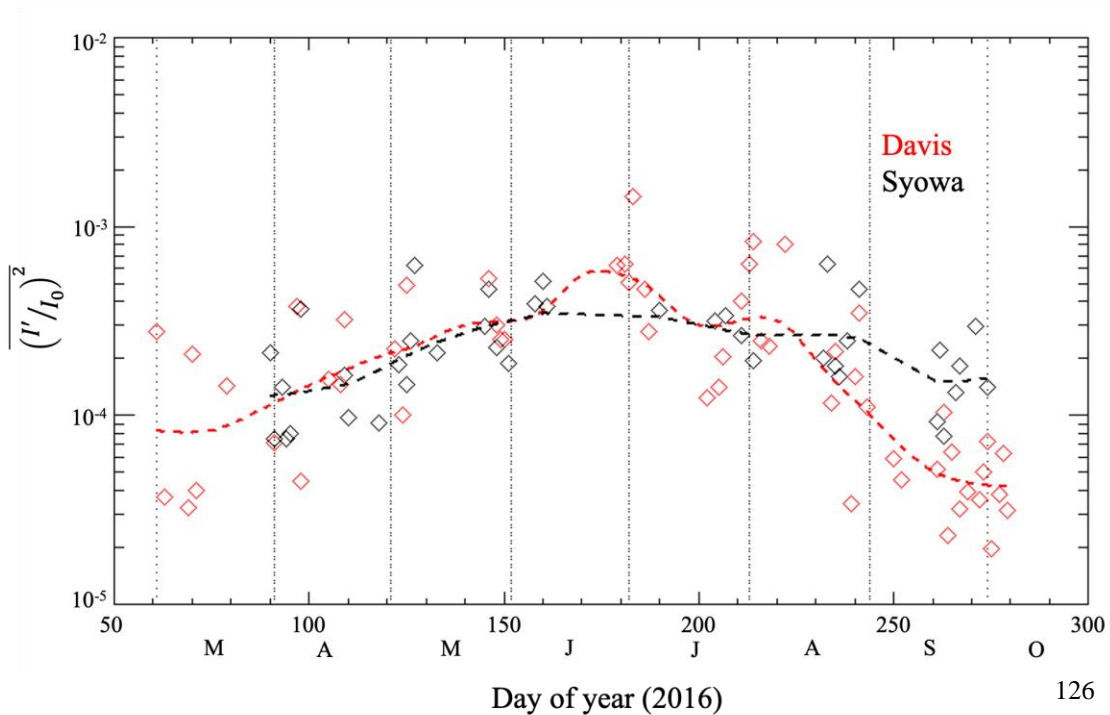
106 each $256 \times 256 \text{ km}^2$ area image, centered on the zenith, with $1 \times 1 \text{ km}^2$ pixel size . The
 107 spectral components with 5-100 km horizontal wavelengths, 8-60 min periods, and $0-150 \text{ ms}^{-1}$
 108 phase speeds were extracted and regarded as representing GW intensities.

109

110 3. Comparison of GW activities between Syowa and Davis

111 Figure 1 shows total powers of the GWs, obtained using the PSD integrated in direction
 112 and phase speed from $0-150 \text{ ms}^{-1}$, over Davis and Syowa stations. The GW activity over both
 113 stations increased from March-April (fall) to May-August (winter) and decreased in September-
 114 October (spring). The total powers have similar seasonal variations, although the power at Davis
 115 was enhanced in late June to early July and late July to early August. On the other hand, the total

116 pow



er
 over
 Dav
 is in
 spri
 ng
 was
 thre
 e
 126 time

127 s smaller than that over Syowa.

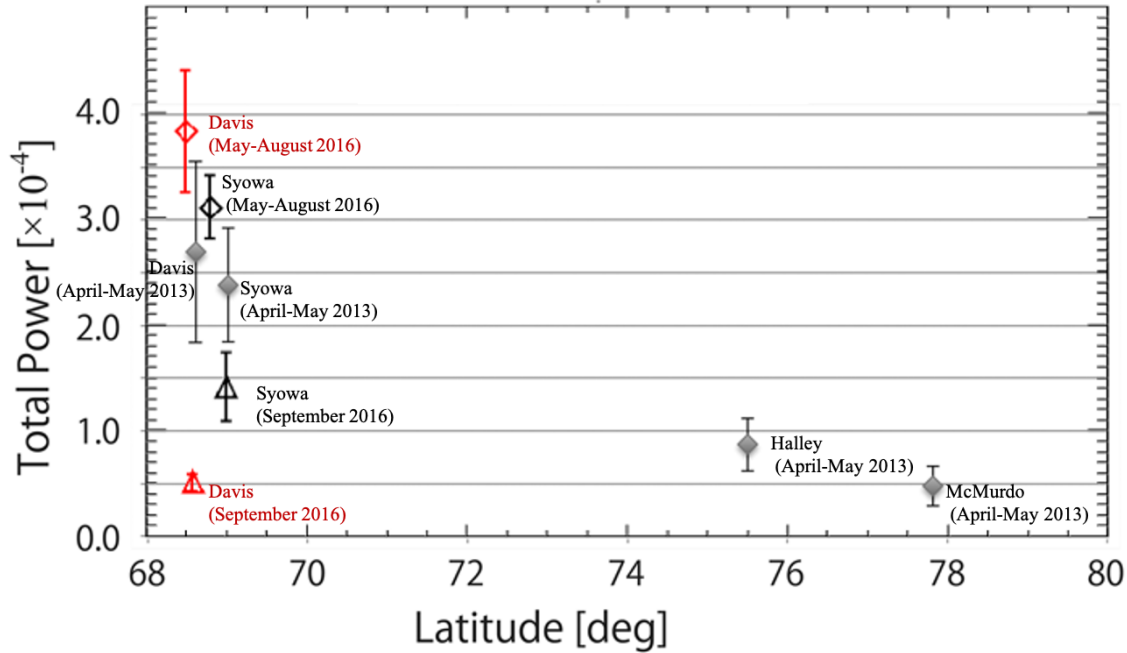
128

129 Figure 1. The red and black diamonds indicate total powers of GWs at Davis and Syowa,
130 respectively. The red and black dashed lines indicate the smoothed total powers with logarithmic
131 Gaussian weighting function ($\sigma = 15$ days, *width* = 61 days), respectively. It should be noted
132 that the smoothed values have large uncertainty because of the sparse data.

133

134 Figure 2 follows Matsuda et al. (2017), but the total powers averaged in May-August and
135 September over Davis and Syowa have been added. The powers over both stations were largest
136 in May-August 2016, followed by April-May 2013 and September 2016. The total powers over
137 Syowa and Davis in May-August, and over Syowa in September are larger than those over
138 Halley and McMurdo in April-May, but the one over Davis in September is comparable.

139 The average power in May-August 2016 over Davis was larger than that over Syowa by
140 7×10^{-5} . This difference was larger than its one standard deviation (5×10^{-5}), which was
141 calculated from one standard deviation of the two average total powers over Syowa and Davis in
142 May-August. However, the powers in April-May 2013 were similar between Davis and Syowa,
143 and Matsuda et al. (2017) concluded that the powers over Syowa and Davis were not different
144 significantly. This contradiction could be attributed to different sampling numbers. The numbers
145 of sampling days in May-August 2016 (23 days at Syowa and 29 days at Davis) are about three
146 times larger than those in April-May 2013 (9 days at Syowa and 8 days at Davis). The
147 confidence intervals in May-August 2016 should be about $\sqrt{3}$ times smaller than those in April-
148 May 2013 in Figure 2. Also, the total power in September over Davis was almost three times
149 (9×10^{-5}) smaller than that over Syowa, and this difference was larger than its standard
150 deviation (3×10^{-5}). Thus, the GW total powers have significant differences between Syowa
151 and Davis.



152

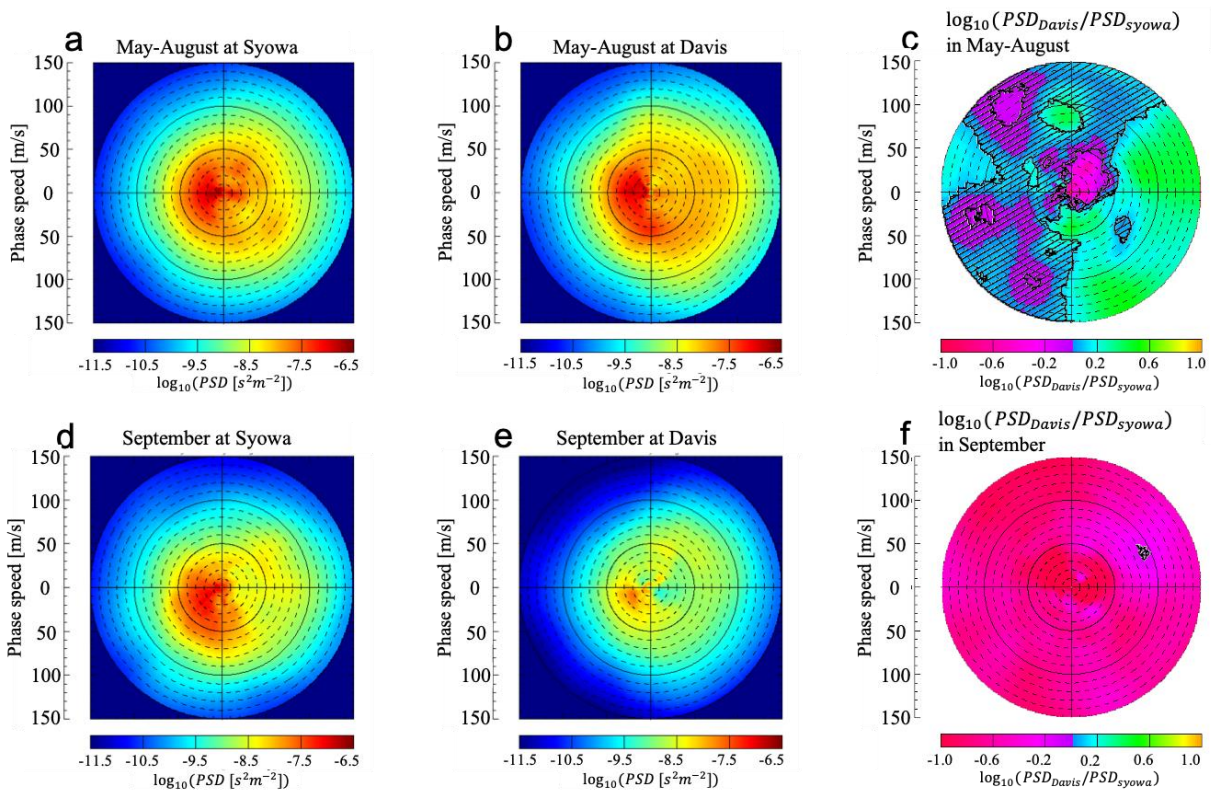
153 Figure 2. The red and black diamonds (triangles) indicate the mean total power in May to August
 154 (September) in Davis and Syowa, respectively. The gray diamonds indicate the mean total
 155 variance in April to May, 2013 [Matsuda et al., 2017]. These diamonds from right to left indicate
 156 the variances in Davis, Syowa, Halley, and McMurdo, respectively. The error bar indicates
 157 confidence interval of the average total power.

158

159 To further explore the different characteristics of the GWs between Davis and Syowa, the
 160 average phase velocity spectra for May-August and September are compared in Figure 3. The
 161 spectra for Syowa and Davis in Figures 3a, b, d, and e have the same directionality; that is, for
 162 phase speeds $\leq \sim 50 \text{ ms}^{-1}$, the PSD between $180 - 360^\circ$ clockwise from the north (westward)
 163 is larger than that in the same speed range between $0 - 180^\circ$ clockwise (eastward). For phase
 164 speeds $\geq 80 \text{ ms}^{-1}$, the result is reversed, and the PSD magnitude is for higher eastward waves.
 165 However, the spectral ratio (PSD_{Davis}/PSD_{Syowa}) in Figure 3c shows the PSD averaged in May-
 166 August around $45 - 180^\circ$ clockwise from the north (northeast to southward), especially

167 $\geq \sim 50 \text{ ms}^{-1}$, is larger over Davis than that over Syowa by one standard deviation in the PSD
 168 difference. This result implies that the larger PSD for azimuth between $45 - 180^\circ$ clockwise
 169 from the north contributed to the higher winter mean total power at Davis. On the other hand, for
 170 September (Figure 3f), the PSD at Davis in September is smaller in almost the whole phase
 171 velocity domain than that in Syowa by one standard deviation, implying the larger PSD in almost
 172 the whole domain contributed to the larger total power at Syowa during the Spring. These
 173 differences can be caused by the two possible mechanisms (1) wind filtering (2) wave
 174 generation. In the following section, we will discuss these mechanisms.

175



176

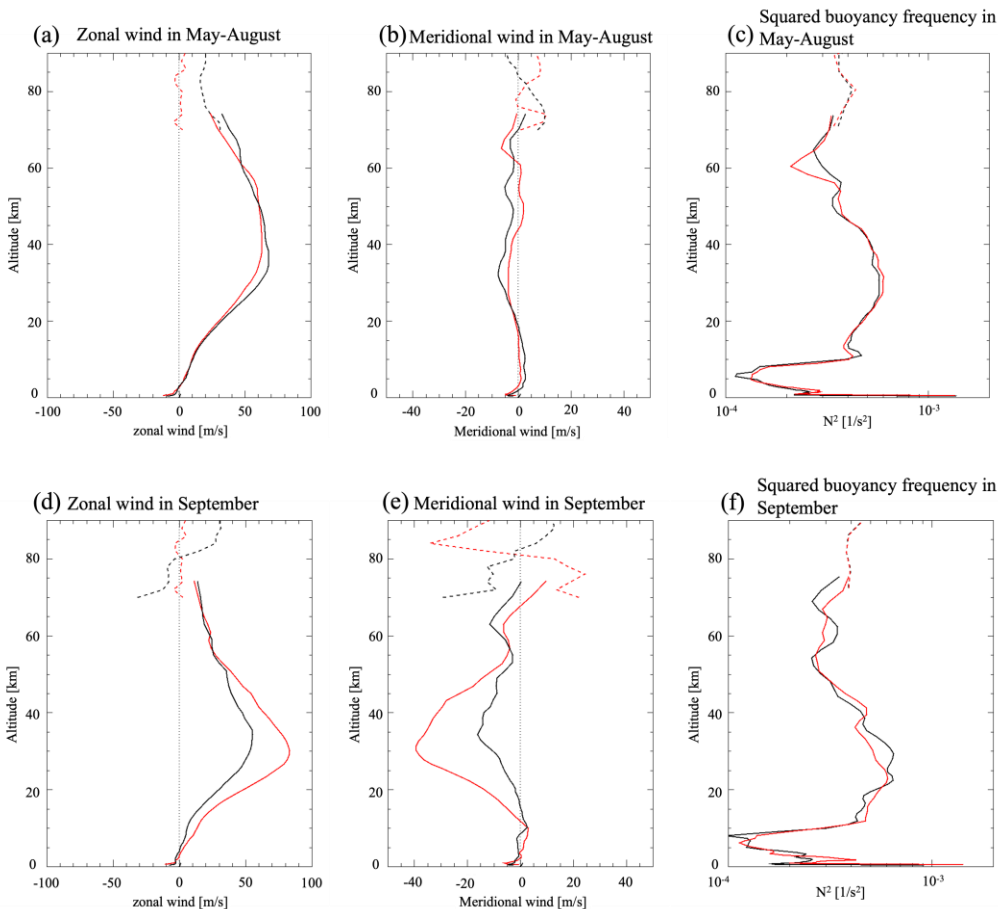
177 Figure 3. PSDs averaged in May-August and September at Syowa (a and b) and Davis (d and e),
 178 respectively. Phase speed lines are separated by 10 m s^{-1} . Panels c and f show the ratio between

179 the PSDs at Syowa and Davis in May-August and September, respectively. The hatch areas
 180 indicate that the ratio is within the confidence interval.

181

182 4. Comparison between GW spectra and transmission diagrams

183 To evaluate the wind filtering effect, the GW spectra were compared with transmission
 184 diagrams. The transmission diagram shows the possibility of vertical propagation, for a GW on a
 185 phase velocity spectrum, from the altitude of a wave emission up to the airglow layer altitude
 186 (Tomikawa, 2015). The wave source and airglow altitudes are assumed to be 10 km and 87 km,
 187 respectively. The diagrams were calculated from the winds and buoyancy frequencies averaged

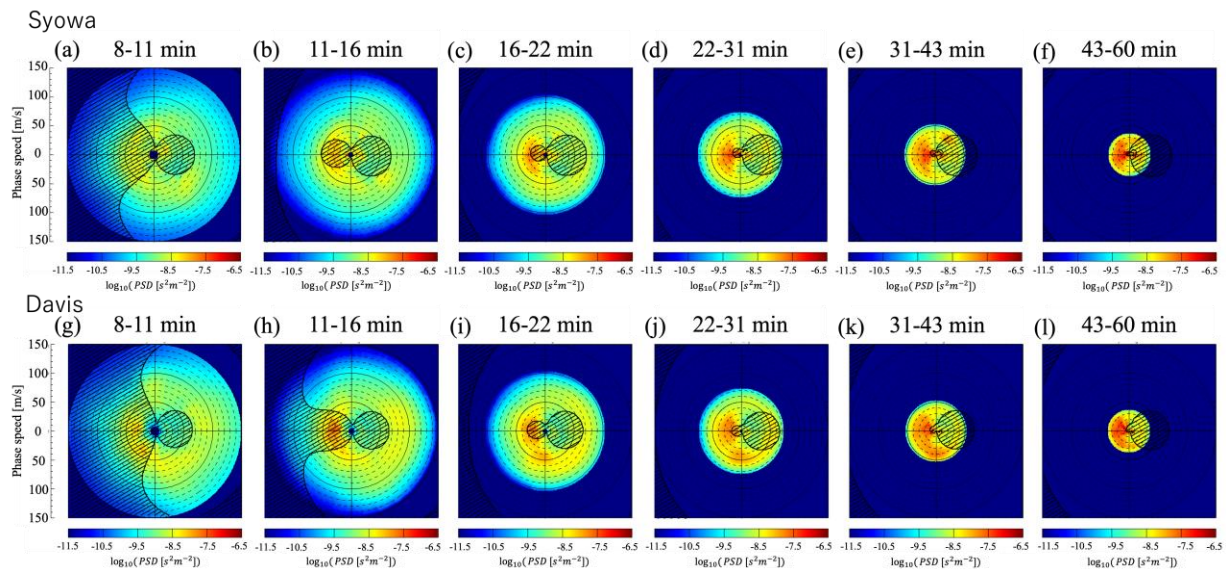


188 in May-August and September at each station (Figure 4).

189 Figure 4. (a) Mean zonal and (b) meridional wind, and (c) squared buoyancy frequency profiles in May
 190 to August in Syowa (black) and Davis (red), respectively. The solid lines indicate re-analysis, MERRA-2.
 191 The dashed lines indicate observations (MF radars and MLS/Aura). (d), (e), and (f) are the same as (a),
 192 (b), and (c), respectively, but in September.

193

194 The winds and buoyancy frequencies below 70 km altitude are from The Modern-Era
 195 Retrospective Analysis for Research and Applications, Version 2, i.e., MERRA-2, (Gelaro et al.,
 196 2017), and those above the top of MERRA-2 were from observations, MF radars (Tsutsumi et
 197 al., 2001) and Aura Microwave Limb Sounder (MLS) (Waters et al., 2006). The values between
 198 70 km and the top of MERRA-2 are averages between MERRA-2 and the observations
 199 calculated with a linear weighting function. Tomikawa (2015) pointed out that the propagation
 200 possibility significantly depends on a GW period so that the spectra in Figure 3 were divided into
 201 6-period bands in accordance with Matsuda et al. (2017).

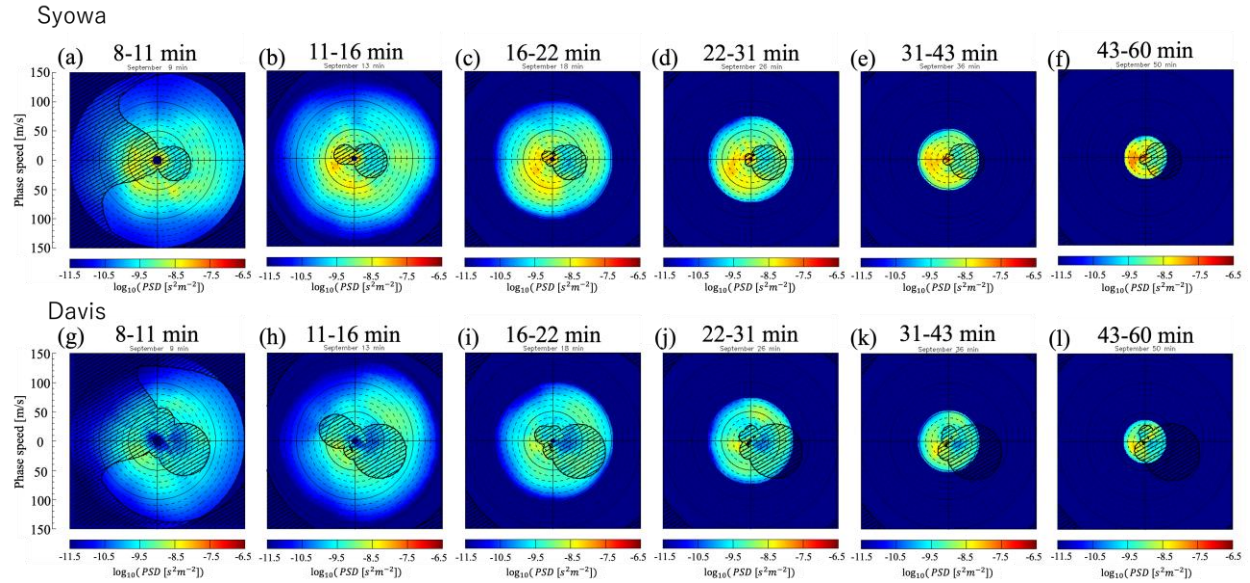


203 Figure 5. Comparison between the average spectra and transmission diagrams in May-August.
204 The color plots indicate the mean spectra in Syowa and Davis in period ranges of 8-11, 11-16,
205 16-22, 22-31, 3-43, and 43-60 min, respectively. The shaded areas indicate prohibited areas for
206 GWs to propagate into the mesopause region.

207

208 Figure 5 shows the comparison between the averaged spectra and transmission diagrams in May-
209 August. The wind filtering effects at each period are almost the same at both stations; that is, the
210 GWs with very short periods tended to be filtered in the westward phase velocity spectra, and the
211 ones with the periods closer to an hour were filtered on the eastward phase velocity spectra less
212 than $\sim 70 \text{ ms}^{-1}$. This result shows that the wind filtering effect cannot explain the larger PSDs in
213 eastward phase velocity in Davis. It should be noted that PSDs in the westward phase velocity
214 spectra less than $\sim 50 \text{ ms}^{-1}$ and 8-16 min periods were enhanced at both stations even though they
215 should be filtered. This result suggests that those GWs were not generated below the assumed 10
216 km source altitude (i.e., the troposphere). Bossert et al. (2017) and Heale et al. (2017) showed
217 that the saturation of large-scale (long period) GWs can generate small-scale secondary GWs in
218 the mesosphere. These saturated waves should also have higher harmonic Fourier components in
219 frequency and horizontal wavenumber domains. The PSDs in period range 31-60 min and
220 westward phase velocity less than $\sim 50 \text{ ms}^{-1}$ were also enhanced suggesting those GWs were
221 saturated such that they might generate the small scale GWs and have higher harmonic Fourier
222 components.

223



224

225 Figure 6 Comparison between the average spectra and transmission diagrams in September. The
 226 color plots indicate the mean spectra in Syowa and Davis in period ranges of 8-11, 11-16, 16-22,
 227 22-31, 31-43, and 43-60 min, respectively. The shaded areas indicate prohibited areas for gravity
 228 waves.

229

230 Figure 6 is the same as Figure 5 but in September. The prohibited spectra in Davis were
 231 broadened into $\sim 70\text{-}90 \text{ ms}^{-1}$ southeastward more widely than those in Syowa because of the
 232 stronger southward wind. This difference between the filtering effects can explain the larger PSD
 233 in $\sim 70\text{-}90 \text{ ms}^{-1}$ southeastward phase velocity area in Syowa but cannot explain the PSD in the
 234 rest of the phase velocity area.

235

236 In summary, the filtering effect cannot explain the difference in May-August but can
 237 somewhat explain that in September. This result implies that other physical mechanisms should
 238 contribute more to the difference in the PSDs between Syowa and Davis. The possible
 mechanisms are (1) Horizontal propagation and (2) Source activity. The next section focuses on

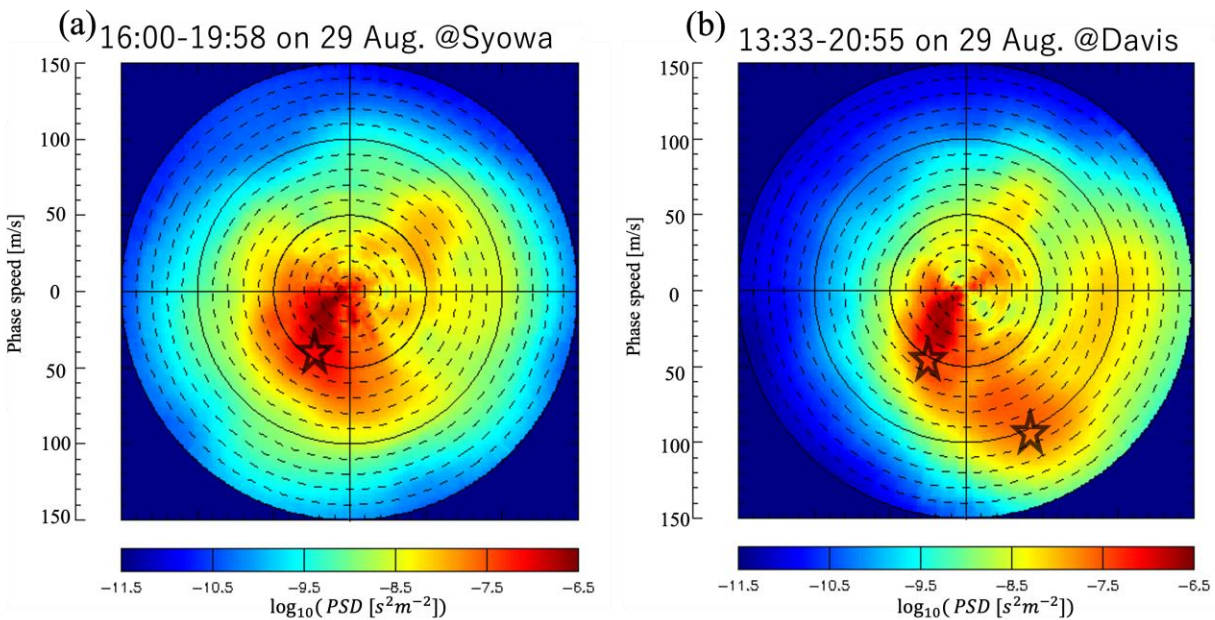
239 an event for GWs with eastward phase velocity at Davis to further explorer the differences in
 240 May-August.

241

242 **5. Event for GWs with high southeastward phase velocity at Davis on August 29, 2016**

243 **5.1. Origin altitudes of GWs on August 29, 2016.**

244 Intense GWs with east to southward ($90 - 180^\circ$ clockwise from the north) phase velocity
 245 higher than $\sim 50 \text{ ms}^{-1}$ were observed at Davis on August 29, 2016, but not observed at Syowa.
 246 Figure7 shows the one-night mean spectra on August 29 at Syowa and Davis. Powers at Syowa
 247 and Davis were intense in southwestward phase velocity spectra with $\sim 20\text{-}30 \text{ ms}^{-1}$, while the
 248 powers at Davis were larger in southeastward phase velocity spectra between $80\text{-}120 \text{ ms}^{-1}$ than
 249 those at Syowa. The features of the two PSDs are similar to those of the winter averages shown
 250 in Figure 3.



251

252 Figure 7. PSDs averaged on August 29, 2016, at Syowa (a) and Davis (b), respectively. The stars
 253 indicates initial phase velocities for raytracing method.

254

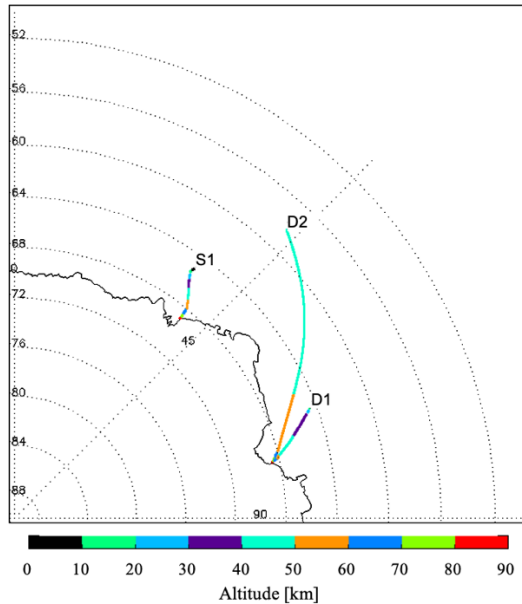
255 To explore where the GWs with $\sim 100 \text{ ms}^{-1}$ southeastward phase velocity came from, we
 256 applied a backward raytracing method (Kogure et al., 2018; Kogure et al., 2020). The initial λ_H ,
 257 τ , C_h are selected as values corresponding to the peaks of the power in $\sim 30 \text{ ms}^{-1}$ southwest
 258 velocity spectra at Syowa and Davis, and $\sim 100 \text{ ms}^{-1}$ southeast velocity spectra at Davis. Table 3
 259 shows the initial parameters. The background wind and temperature below 70 km altitude were
 260 obtained from MERRA-2. Above the top of MERRA-2 ($\sim 74 \text{ km}$ altitude), the background wind
 261 was measured by MF radars, and the temperature was measured from Aura MLS. Between 70
 262 km and the top of MERRA-2, a linear weighting function was used to average between MERRA-
 263 2 and the observations. It should be noted that horizontal wind shear effects on wavelength were
 264 neglected above the top of MERRA-2.

	No.	λ_H [km]	τ [min]	C_h [m/s]	Direction [degree]	Terminal height [km]
Syowa	S1	84	30	46	209	0.1
Davis	D1	28	9	52	207	9.2
	D2	88	14	103	156	44.5

265

266 Table 3. Initial raytracing parameters for hydroxyl layer gravity waves

August 29 2016



267

268 Figure 8. The backward raytracing method results for the GWs described in Table 3.

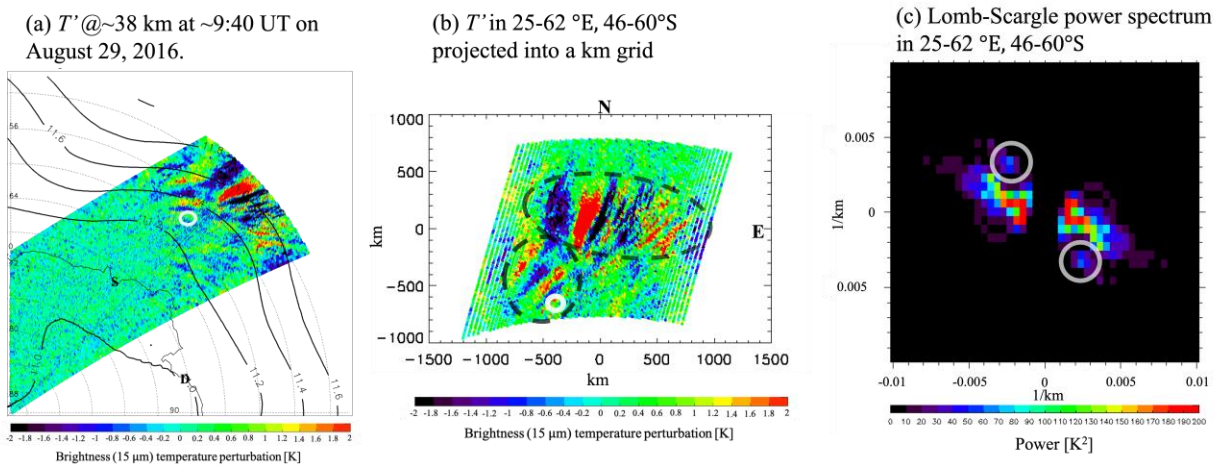
269

270 The backward raytracing results in Figure 8 show the three GWs propagated from the southern
 271 ocean. While the S1 and D1 (southwestward phase velocities) can propagate from 0.1 and 9.2 km
 272 altitudes, respectively, the D2 (southeastward phase velocity) back trace terminated at 44.5 km
 273 altitude because of a critical level. This result indicates that D2 could not have originated from
 274 below that level and must have been generated in the upper stratosphere. Rourke et al. (2017)
 275 observed such gravity waves with eastward phase velocity over Davis. This work also showed
 276 that those waves originated from the upper stratosphere by using the raytracing method, although
 277 it used empirical model background fields and did not determine the wave sources.

278 **5.2. The possible GW sources in the stratosphere.**

279 The possible sources for the D2 GW (southeastward phase velocity) in the stratosphere
 280 are (1) spontaneous adjustment (Plougonven and Zhang, 2014), and (2) secondary wave

281 generation (Vadas & Becker, 2019; Kogure et al., 2020). The residual of the nonlinear balance
 282 equation (ΔNBE) from Plougonven and Zhang (2014) using MERRA-2 fields was not enhanced
 283 around the termination point so that the spontaneous adjustment mechanism can be ruled out (not
 284 shown). On the other hand, the Atmospheric Infrared Sounder (AIRS) aboard NASA's Aqua
 285 satellite captured two intense GWs near the termination point ($\sim 42^\circ\text{E}$, $\sim 58^\circ\text{S}$) at $\sim 9:40$ UT in the
 286 $15\ \mu\text{m}$ high channel, which, in the polar region, is most sensitive to GW temperature
 287 perturbations at ~ 38 km altitude (Figure 9 (a)). (Channel response data can be acquired from
 288 https://datapub.fz-juelich.de/slcs/airs/gravity_waves/ (Hoffman et al., 2013; 2017)). The $15\ \mu\text{m}$
 289 low channel of AIRS, which is most sensitive to GW temperature perturbation at ~ 23 km altitude,
 290 also captured two intense GWs in a similar area (not shown). These observed GWs appeared in
 291 the leeward of the geopotential height ridge at 200 hPa suggesting the waves were emitted from
 292 the tropospheric jet through spontaneous adjustment (Plougonven and Zhang, 2014).



293
 294 Figure 9. (a) Temperature perturbations observed by AIRS at ~ 38 km altitude at $\sim 9:40$ UT on
 295 August 29, 2016. The contour shows geopotential heights at 200 hPa. The white
 296 circle corresponds to the termination of the D2 wave. (b) The Temperature perturbations in $25-$
 297 62°E , $46-60^\circ\text{S}$ projected onto a km grid. The white circle indicates the terminal point of the D2

298 GW (with southeastward phase velocity observed over Davis). (c) The Lomb-Scargle power
299 spectrum of the temperature perturbations in 25-62°E, 46-60°S .

300

301 The AIRS data were projected onto a km grid in Figure 9 (b). There are two GWs apparent, with
302 ~500 km and ~200 km horizontal wavelengths. The GW with ~200 km horizontal wavelength is
303 situated near the termination of the D2 ray. Such intense GWs observed by AIRS could be
304 saturated and have generated secondary gravity waves in the upper stratosphere and the
305 mesosphere due to shear and/or convective instabilities (Bossert et al., 2015; Heale et al., 2020;
306 Kogure et al., 2020). To investigate the saturation of the GWs, we calculate the local Richardson
307 number, Ri , along a forward ray path. This analysis is similar to Kogure et al. (2020) with the
308 exception that this study assumes wave action conservation; previously it was assumed that the
309 growth rate of wave amplitude was the square root of density. To determine an initial horizontal
310 vector for the forward raytracing, the AIRS data in Figure 9(b) is subject to 2D Lomb-Scargle
311 spectral analysis. Figure 9(c) shows the Lomb-Scargle power spectrum where two local maxima
312 in the spectrum can be seen. The local power maxima with 241 km horizontal wavelength and a
313 direction of 146° or 214° clockwise from north correspond to the GW with ~200 km horizontal
314 wavelength in Figure 9(b). The 2D Lomb-Scargle analysis has 180° ambiguity, but 146° is
315 adopted here because the phase speed of a GW emitted from a jet is expected to match the phase
316 speed of a baroclinic wave, i.e., eastward (Plougonven and Snyder, 2007). Murphy et al.(2014)
317 also frequently observed GWs in radiosonde data with eastward phase velocity, which were
318 potentially emitted from the jet, in the lower stratosphere over Davis but rarely observed
319 westward GWs.

320 The measured amplitude of the GW with a 241 km horizontal wavelength is ~ 2 K in Figure 9(a)
321 and (b), but this drastically underestimates the true amplitude (Hoffman et al., 2013; 2017). A
322 response rate of the AIRS high 15 μm kernel is estimated using the AIRS vertical kernel
323 investigation (https://datapub.fz-juelich.de/slcs/airs/gravity_waves/data/kernel.pdf), and the
324 amplitude of the raytraced GW was compensated accordingly. However, the response rate and
325 peak of the AIRS kernel varies in location and season, which causes ambiguities of the amplitude
326 and the altitude used to launch the ray. Due to these ambiguities, the response rate and the initial
327 altitude are varied by 3% and 2 km, respectively. The AIRS instrument cannot observe wave
328 period, but the GWs emitted from jets tend to have a long ground-based period. Here, the period
329 was trialled at 3, 5, and 10 hours.

330 The altitudes at which $R_i < 0.25$ for the trial GWs, which corresponding to potential start
331 of saturation, are given in Table 4. Figure 10 shows the forward raytracing result for the GW
332 with 3 hour ground-based period from 38 km altitude. This GW began to be saturated at almost
333 the same point (diamond mark) as the D2 termination (white circle) on the horizontal surface
334 although the saturation altitude is ~ 3 km higher than the D2 termination altitude. Precise
335 agreement between the D2 termination height and the saturation height is not needed because the
336 D2 wave could have been launched above the backward ray tracing termination height (but not
337 below). GWs launched from similar horizontal positions but with the other parameters also
338 propagated in the same direction (i.e., Davis ward) but the propagation paths and saturation
339 altitudes varied. The saturation altitude of the GWs with the 3 hour ground-based period was
340 closer to altitudes of the D2 path than those for 5 and 10 hours. It should be noted that Murphy et
341 al. (2014) occasionally observed GWs with eastward and 22 ms^{-1} phase speed (from 241 km/3
342 hours) in the lower stratosphere over Davis that are consistent with this wave. Making the

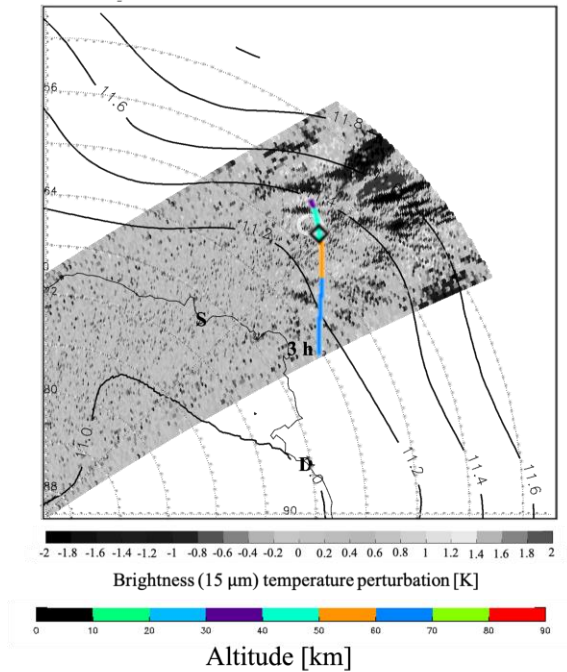
343 assumption that the southeast propagating GW in the AIRS data had ~3 hour period, it can be
 344 asserted that the wave saturated at ~45-50 km. Since characteristic scales and directions of a
 345 secondary GW depend on a half scale and direction of a local body force, respectively (Vadas et
 346 al., 2003; Heale et al., 2020), the jet GW could cause a local body force with southeastward
 347 direction and ~44 km horizontal scale (a half of D2 GW horizontal wavelength). This local body
 348 force could create the GWs with $\sim 100 \text{ ms}^{-1}$ southeastward phase velocity. Otherwise, the GWs
 349 over Davis could be generated through nonlinear fluid interactions (Andreassen et al., 1998;
 350 Bossert et al., 2015; Fritts et al., 1994, 1998; Heale 2017). Thus, the GWs with $\sim 100 \text{ ms}^{-1}$
 351 southeastward phase velocity over Davis were very likely secondary GWs generated by the

Period (hour)	Initial altitude	Response rate of AIRS kernel (%)	Initial amplitude (K)	Bottom height Ri < 0.25 (km)	Initial vertical wavelength (km)
3	36	10 (7, 13)	20 (29, 15)	46 (39, 49)	16
3	38	10 (7, 13)	20 (29, 15)	48 (41, 59)	16
3	40	10 (7, 13)	20 (29, 15)	49 (46, 51)	16
5	36	14 (11, 17)	14 (18, 12)	50 (48, 51)	18
5	38	16 (13, 19)	13 (15, 11)	51 (51, 53)	19
5	40	16 (13, 19)	13 (15, 11)	53 (52, 56)	19
10	36	17 (14, 20)	12 (14,10)	52 (51,53)	20
10	38	19 (16, 22)	11 (13, 9)	55 (53, 57)	21
10	40	19 (16, 22)	11 (13, 9)	57 (55, 59)	21

352 intense GW activity above the southern ocean.

353 Table 4. Parameters for GW with a 241 km horizontal wavelength in the AIRS data on August
 354 29, 2016. The initial amplitudes are 2 K (which is observed by AIRS) \times the inverse of the
 355 response rate of the AIRS vertical kernel based on Figure 1 in Hoffmann et al. (2017). The
 356 values in parentheses are corresponding to the response rate -3% and $+3 \%$, respectively.

357



358

359 Figure 10. Raytracing result for the GWs with southeast horizontal wavevector superimposed in

360 Figure 9(a). Its ground-based period, initial height, and initial temperature amplitude were

361 assumed as 3 hour, 38 km, and 20 K, respectively. The diamond indicates a bottom altitude

362 with $Ri < 0.25$.

363

364

6. Conclusion

365 We compared the GW total powers and phase velocity spectra in the OH layer at two

366 Antarctic stations, Davis and Syowa, from March to October 2016. The total powers showed

367 maxima in winter and have similar seasonal variation at both stations. The powers at Davis were

368 one standard deviation higher in winter and three times smaller in September than those at

369 Syowa, respectively, although Matsuda et al. (2017) concluded that the powers at both stations

370 were not significantly different at those times in 2013. This contradiction could be attributed to

371 different sampling numbers, as our sampling numbers are about three times larger than those in

372 Matsuda et al. (2017). The larger total power at Davis in winter was attributed to GWs with high

373 eastward ($\geq \sim 50 \text{ ms}^{-1}$) phase velocity. On the other hand, the larger total power at Syowa in
374 September was attributed to GWs with omnidirectional phase velocity. To evaluate background
375 meteorological field impacts on the GWs at both stations, we compared the spectra and
376 transmission diagrams and then concluded that filtering effects cannot explain the differences in
377 May-August but somewhat explain them in September. To further explore the causes of the
378 differences between Syowa and Davis in May-August, we focused on a GW event with eastward
379 phase velocity at Davis. The raytracing method indicated that those GWs propagated from ~ 45
380 km altitude over the southern ocean ($\sim 43^\circ\text{E}$, $\sim 58^\circ\text{S}$), where GWs emitted from the tropospheric
381 jet were apparent. These tropospheric jet GWs were probably saturated in 45-50 km altitudes and
382 caused a ~ 44 km horizontal scale (a half of the GW horizontal wavelength over Davis) local
383 southeastward body force. Otherwise, the GWs over Davis could be generated through nonlinear
384 fluid interactions. Therefore, the GWs with eastward phase velocity observed in the mesosphere
385 were secondary gravity waves. This result suggests that the larger PSD in eastward phase
386 velocity at Davis in May-August was attributed to secondary GWs, that secondary GWs may
387 contribute to GW phase velocity spectra in the mesosphere and that they cause non-negligible
388 GW longitudinal variations. The larger total power in Syowa in September might be attributed to
389 differences in a GW source activity or/and generation mechanisms between Syowa and Davis,
390 but further study is needed to verify this.

391 **Acknowledgments, Samples, and Data**

392 This work is supported by the JSPS grant JRPs-LEAD with DFG program, JSPS KAKENHI
393 Grant Number 19K23465, JSPS Overseas Challenge Program for Young Researchers (No.
394 201780038), and the Scientific Committee on Antarctic Research (SCAR) fellowship award
395 2019. Support for the operation of the Davis MF radar and its analysis was provided through

396 AAS project number 4025, 4056 and 4445. The USU all-sky OH imager operated at Davis
397 Station and its data analysis are supported by NSF #1143587 and NSF # 1443730. MERRA-2
398 data were obtained at <http://disc.sci.gsfc.nasa.gov>. MLS_Aura data were obtained at
399 <https://mls.jpl.nasa.gov/index-eos-mls.php>. The AIRS/Aqua gravity wave data sets (Hoffmann et
400 al., 2017) are provided by Forschungszentrum Jülich ([https://datapub.fz-
401 juelich.de/slcs/airs/gravity_waves/data](https://datapub.fz-juelich.de/slcs/airs/gravity_waves/data)). The daily average phase velocity spectra data at both
402 stations can be obtained at <http://id.nii.ac.jp/1291/00016369/>. The MF radar data averaged in
403 winter and September can be obtained at <http://id.nii.ac.jp/1291/00016368/> . The M-transform
404 program can be obtained at <http://polaris.nipr.ac.jp/~airglow/M-transform/>.
405

406

407 **References**

- 408 Alexander, M.J., Geller, M., McLandress, C., Polavarapu, S., Preusse, P., Sassi, F., Sato, K., et
409 al. (2010). Recent developments in gravity-wave effects in climate models and the global
410 distribution of gravity-wave momentum flux from observations and models. *Quarterly*
411 *Journal of the Royal Meteorological Society.*, 136: 1103-1124, doi:10.1002/qj.637.
- 412 Alexander, S. P., A. R. Klekociuk, & T. Tsuda (2009), Gravity wave and orographic wave
413 activity observed around the Antarctic and Arctic stratospheric vortices by the COSMIC
414 GPS-RO satellite constellation, *Journal of Geophysical Research.*, 114, D17103,
415 doi:10.1029/2009JD011851.
- 416 Andreassen, Ø., Hvidsten, P., Fritts, D., & Arendt, S. (1998). Vorticity dynamics in a breaking
417 internal gravity wave. Part 1. Initial instability evolution. *Journal of Fluid Mechanics*, 367,
418 27–46. doi: 10.1017/S0022112098001645
- 419 Baker, D. J., & Stair Jr, A. T. (1988). Rocket measurements of the altitude distributions of the
420 hydroxyl airglow. *Physica scripta*, 37(4), 611, doi: 10.1088/0031-8949/37/4/021
- 421 Bossert, K., Fritts, D. C., Pautet, P.-D., Williams, B. P., Taylor, M. J., Kaifler, B., Dörnbrack, A.,
422 et al. (2015), Momentum flux estimates accompanying multiscale gravity waves over
423 Mount Cook, New Zealand, on 13 July 2014 during the DEEPWAVE campaign, *Journal of*
424 *Geophysical Research: Atmospheres*, 120, 9323– 9337, doi:10.1002/2015JD023197.
- 425 Bossert, K., Kruse, C. G., Heale, C. J., Fritts, D. C., Williams, B. P., Snively, J. B., Pautet, P.-D.,
426 and Taylor, M. J. (2017), Secondary gravity wave generation over New Zealand during the

- 427 DEEPWAVE campaign, *J. Geophys. Res. Atmos.*, 122, 7834–7850,
428 doi:10.1002/2016JD026079.
- 429 Bossert, K., Fritts, D. C., Pautet, P.-D., Williams, B. P., Taylor, M. J., Kaifler, B., et al. (2015).
430 Momentum flux estimates accompanying multiscale gravity waves over mount cook, New
431 Zealand, on 13 July 2014 during the DEEPWAVE campaign. *Journal of Geophysical*
432 *Research: Atmospheres*, 120, 9323–9337. doi: 10.1002/2015JD023197.
- 433 Fritts, D. C., & Alexander, M. J. (2003), Gravity wave dynamics and effects in the middle
434 atmosphere, *Reviews of Geophysics*, 41, 1003, doi:10.1029/2001RG000106, 1.
- 435 Fritts, D. C., Arendt, S., & Anderassen, Ø. (1998). Vorticity dynamics in a breaking internal
436 gravity wave. Part 2. Vortex interactions and transition to turbulence. *Journal of Fluid*
437 *Mechanics*, 367, 47–65. doi: 10.1017/S0022112098001633
- 438 Fritts, D. C., Isler, J. R., & Andreassen, Ø. (1994). Gravity wave breaking in two and three
439 dimensions: 2. Three-dimensional evolution and instability structure. *Journal of*
440 *Geophysical Research*, 99(D4), 8109–8123. doi: 10.1029/93JD03436
- 441 Fritts, D. C., & Vincent, R. A. (1987). Mesospheric Momentum Flux Studies at Adelaide,
442 Australia: Observations and a Gravity Wave–Tidal Interaction Model, *Journal of*
443 *Atmospheric Sciences*, 44(3), 605-619, doi:10.1175/1520-
444 0469(1987)044<0605:MMFSAA>2.0.CO;2
- 445 Gelaro, R., McCarty, W., Suárez, M. J., Todling, R., Molod, A., Takacs, L., Randles, C. A., et al.
446 (2017). The Modern-Era Retrospective Analysis for Research and Applications, Version 2
447 (MERRA-2), *Journal of Climate*, 30(14), 5419-5454, doi: 10.1175/JCLI-D-16-0758.1.

- 448 Grygalashvyly, M., Sonnemann, G. R., Lübken, F.-J., Hartogh, P., and Berger, U. (2014),
449 Hydroxyl layer: Mean state and trends at midlatitudes, *J. Geophys. Res. Atmos.*, 119,
450 12,391– 12,419, doi:10.1002/2014JD022094.
- 451 Heale, C. J., Bossert, K., Snively, J. B., Fritts, D. C., Pautet, P.-D., and Taylor, M. J. (2017),
452 Numerical modeling of a multiscale gravity wave event and its airglow signatures over
453 Mount Cook, New Zealand, during the DEEPWAVE campaign, *J. Geophys. Res. Atmos.*,
454 122, 846– 860, doi:10.1002/2016JD025700.
- 455 Heale, C. J., Bossert, K., Vadas, S. L., Hoffmann, L., Dörnbrack, A., Stober, G., B. Snively, et al.
456 (2020). Secondary gravity waves generated by breaking mountain waves over Europe.
457 *Journal of Geophysical Research: Atmospheres*, 125, e2019JD031662,
458 doi:10.1029/2019JD031662
- 459 Hoffmann, L., X. Xue, & M. J. Alexander. (2013). A global view of stratospheric gravity wave
460 hotspots located with Atmospheric Infrared Sounder observations, *Journal of*
461 *Geophysical Research: Atmospheres*, 118, 416-434, doi:10.1029/2012JD018658.
- 462 Hoffmann, L., Spang, R., Orr, A., Alexander, M. J., Holt, L. A., & Stein, O. (2017), A decadal
463 satellite record of gravity wave activity in the lower stratosphere to study polar
464 stratospheric cloud formation, *Atmospheric Chemistry and Physics*, 17, 2901-2920,
465 doi:10.5194/acp-17-2901-2017.
- 466 Kaifler, B., F. J. Lübken, J. Höffner, R. J. Morris, and T. P. Viehl (2015), Lidar observations of
467 gravity wave activity in the middle atmosphere over Davis (69°S, 78°E), *Journal of*
468 *Geophysical Research: Atmospheres*, 120, 4506– 4521, doi:10.1002/2014JD022879.

- 469 Kogure, M., Nakamura, T., Ejiri, M. K., Nishiyama, T., Tomikawa, Y., Tsutsumi, M., Suzuki, et
470 al. (2017). Rayleigh/Raman lidar observations of gravity wave activity from 15 to 70 km
471 altitude over Syowa (69°S, 40°E), the Antarctic, *Journal of Geophysical Research:*
472 *Atmospheres*, 122, 7869– 7880, doi:10.1002/2016JD026360.
- 473 Kogure, M., Nakamura, T., Ejiri, M. K., Nishiyama, T., Tomikawa, Y., & Tsutsumi, M. (2018).
474 Effects of horizontal wind structure on a gravity wave event in the middle atmosphere
475 over Syowa (69°S, 40°E), the Antarctic. *Geophysical Research Letters*, 45, 5151– 5157.
476 doi:10.1029/2018GL078264.
- 477 Kogure, M., Yue, J., Nakamura, T., Hoffmann, L., Vadas, S. L., Tomikawa, Y., et al. (2020).
478 First direct observational evidence for secondary gravity waves generated by mountain
479 waves over the Andes. *Geophysical Research Letters*, 47, e2020GL088845.
480 Doi:10.1029/2020GL088845
- 481 Matsuda, T. S., Nakamura, T., Ejiri, M. K., Tsutsumi, M., and Shiokawa, K. (2014), New
482 statistical analysis of the horizontal phase velocity distribution of gravity waves observed
483 by airglow imaging, *Journal of Geophysical Research: Atmospheres.*, 119, 9707– 9718,
484 doi:10.1002/2014JD021543.
- 485 Matsuda, T. S., Nakamura, T., Ejiri, M. K., Tsutsumi, M., Tomikawa, Y., Taylor, M. J., Zhao,
486 Y., Pautet, P.-D., Murphy, D. J., and Moffat-Griffin, T. (2017), Characteristics of
487 mesospheric gravity waves over Antarctica observed by Antarctic Gravity Wave
488 Instrument Network imagers using 3-D spectral analyses, *Journal of Geophysical*
489 *Research: Atmospheres*, 122, 8969– 8981, doi:10.1002/2016JD026217.

- 490 Murphy, D. J., Alexander, S. P., Klekociuk, A. R., Love, P. T., and Vincent, R. A. (2014),
491 Radiosonde observations of gravity waves in the lower stratosphere over Davis,
492 Antarctica, *J. Geophys. Res. Atmos.*, 119, 11,973– 11,996, doi:10.1002/2014JD022448.
- 493 Nappo, C. J. (2013). An introduction to atmospheric gravity waves. *Academic press*.
- 494 Nishiyama, T., Taguchi, M., Suzuki, H., Dalin, P., Ogawa, Y., Brändström, T., et al.
495 (2021), Temporal evolutions of N₂⁺ Meinel (1,2) band near 1.5.µm associated with aurora
496 breakup and their effects on mesopause temperature estimations from OH Meinel (3,1)
497 band. *Earth Planets Space* **73**, 30, doi:10.1186/s40623-021-01360-0
- 498 Plougonven, R., & Snyder, C. (2007). Inertia–Gravity Waves Spontaneously Generated by Jets
499 and Fronts. Part I: Different Baroclinic Life Cycles, *Journal of the Atmospheric Sciences*,
500 64(7), 2502-2520. doi: 10.1175/JAS3953.1
- 501 Plougonven, R., and Zhang, F. (2014), Internal gravity waves from atmospheric jets and fronts,
502 *Reviews of Geophysics*, 52, 33– 76, doi:10.1002/2012RG000419.
- 503 Rourke, S., Mulligan, F. J., French, W. J. R., & Murphy, D. J. (2017). A climatological study of
504 short-period gravity waves and ripples at Davis Station, Antarctica (68°S, 78°E), during
505 the (austral winter February–October) period 1999–2013. *Journal of Geophysical*
506 *Research: Atmospheres*, 122. doi:10.1002/2017JD026998
- 507 Septi Perwitasari, Takuji Nakamura, Masaru Kogure, Yoshihiro Tomikawa, Mitsumu K. Ejiri,
508 Kazuo Shiokawa (2018), Comparison of gravity wave propagation directions observed by
509 mesospheric airglow imaging at three different latitudes using the M-transform, *Annales*
510 *Geophysicae*, 36, 6, (1597-1605), doi: 10.5194/angeo-36-1597-2018.

- 511 Tomikawa, Y. (2015), Gravity wave transmission diagram, *Annales Geophysicae*, 33, 1479–
512 1484, doi:10.5194/angeo-33-1479-2015.
- 513 Tsutsumi, M., Aso, T. and Ejiri, M.. (2001), Initial results of Syowa MF radar observations in
514 Antarctica, *Adv. Polar Upper Atmosphere research*, 15, 103-116,
515 doi:10.15094/00006333.
- 516 Vadas, S. L., and Becker, E. (2019). Numerical modeling of the generation of tertiary gravity
517 waves in the mesosphere and thermosphere during strong mountain wave events over the
518 Southern Andes. *Journal of Geophysical Research: Space Physics*, 124, 7687– 7718.
- 519 Vadas, S. L., Fritts, D. C., & Alexander, M. J. (2003). Mechanism for the generation of
520 secondary waves in wave breaking regions. *Journal of the Atmospheric Sciences*, 60(1),
521 194–214. doi: 10.1175/1520-0469(2003)060<0194:MFTGOS>2.0.CO;2
- 522 Waters, J. W., Froidevaux, L., Harwood, R. S., Jarnot, R. F., Pickett, H. M., Read, W. G., Siegel,
523 P. H., et al. (2006). The Earth observing system microwave limb sounder (EOS MLS) on
524 the aura Satellite, in *IEEE Transactions on Geoscience and Remote Sensing*, 44, 5, 1075-
525 1092, doi: 10.1109/TGRS.2006.873771.
- 526